Check for updates

ADVANCED ENERGY MATERIALS
www.advenergymat.de

Sub-0.6 eV Inverted Metamorphic GaInAs Cells Grown on Inp and GaAs Substrates for Thermophotovoltaics and Laser Power Conversion

Kevin L. Schulte, Daniel J. Friedman, Titilope Dada, Harvey L. Guthrey, Edgard W. Costa, Eric J. Tervo, Ryan M. France, John F. Geisz, and Myles A. Steiner*

Inverted metamorphic $Ga_{0.3}In_{0.7}As$ photovoltaic converters with sub-0.60 eV bandgaps grown on InP and GaAs are presented. Threading dislocation densities are $1.3 \pm 0.6 \times 10^6$ and $8.9 \pm 1.7 \times 10^6$ cm^{-2} on InP and GaAs, respectively. The devices generate open-circuit voltages of 0.386 and 0.383 V, respectively, under irradiance producing a short-circuit current density of ≈10 A cm^{-2}, yielding bandgap-voltage offsets of 0.20 and 0.21 V. Power and broadband reflectance measurements are used to estimate thermophotovoltaic (TPV) efficiency. The InP-based cell is estimated to yield 1.09 W cm^{-2} at 1100 °C versus 0.92 W cm^{-2} for the GaAs-based cell, with efficiencies of 16.8 versus 9.2%. The efficiencies of both devices are limited by sub-bandgap absorption, with power weighted sub-bandgap reflectances of 81% and 58%, respectively, the majority of which is assumed to occur in the graded buffers. The 1100 °C TPV efficiencies are estimated to increase to 24.0% and 20.7% in structures with the graded buffer removed, if previously demonstrated reflectance is achieved. These devices also have application to laser power conversion in the 2.0–2.3 µm atmospheric window. Peak laser power converter efficiencies of 36.8% and 32.5% are estimated under 2.0 µm irradiances of 1.86 and 2.81 W cm^{-2}, respectively.

1. Introduction

Emerging applications such as thermal energy storage,[1] waste heat recovery,[2,3] small modular nuclear reactors,[4] and portable power generation[5] require thermophotovoltaic (TPV) converters that collect photons of 2 µm and longer wavelengths. Some thermal energy storage applications using TPVs operate at high temperatures (>1500 °C) and can use devices with designs adapted from photovoltaics applications,[6] but there are also potentially impactful applications, for example waste heat recovery, for converters with significantly lower bandgaps to access heat sources at temperatures around 1000 °C or lower. Interest in laser power beaming is also growing, and there is an atmospheric window from 2.0–2.3 µm[7] where high efficiency laser power converters (LPCs) operating in that bandgap range could be useful when coupled with Ho:YAG or Tm fiber lasers emitting at these wavelengths.[8] Converters using the quaternary alloy $Ga_xIn_{1-x}As_ySb_{1-y}$, lattice-matched to a GaSb substrate are one option at these wavelengths, but challenges in the epitaxy of these materials limit their performance.[9,10]

The $Ga_xIn_{1-x}As$ alloy enables access to bandgaps between 1.42 and 0.35 eV and is a common choice for these applications because it can be grown epitaxially with low defect density.[9] 0.74 eV $Ga_{0.47}In_{0.53}As$ devices are grown lattice-matched to InP,[11] while lower bandgaps require graded buffers to shift the lattice constant and access metamorphic $Ga_xIn_{1-x}As$ compositions. Upright photovoltaic cells with bandgaps as low as ≈0.5 eV were developed on InP using InP_yAs_{1-y} or $Ga_xIn_{1-x}As$ compositionally graded buffers.[12–15]

A crucial component of achieving high TPV efficiency is to return unused, sub-bandgap photons, which do not contribute to PV power generation, back to the thermal source. Instead of passing through the device unabsorbed, or being absorbed as a parasitic loss in the device, these photons are reflected back to the emitter, reducing transmission loss and reheating the emitter. An elegant approach to doing this, which has been long understood and practiced,[15] is to implement broadband reflectors behind thin-film devices. Recently, major increases in TPV efficiency were achieved by combining this approach with methods for achieving very high above-bandgap photovoltaic performance.[16–18] Previous <0.74 eV metamorphic $Ga_xIn_{1-x}As$

K. L. Schulte, D. J. Friedman, H. L. Guthrey, E. W. Costa, R. M. France, J. F. Geisz, M. A. Steiner
National Renewable Energy Laboratory
Golden, CO 80401, USA
E-mail: kevin.schulte@nrel.gov

T. Dada, E. J. Tervo
Department of Electrical and Computer Engineering
University of Wisconsin-Madison
Madison, WI 53706, USA

The ORCID identification number(s) for the author(s) of this article can be found under https://doi.org/10.1002/aenm.202303367

© 2024 The Authors. Advanced Energy Materials published by Wiley-VCH GmbH. This is an open access article under the terms of the Creative Commons Attribution-NonCommercial-NoDerivs License, which permits use and distribution in any medium, provided the original work is properly cited, the use is non-commercial and no modifications or adaptations are made.

DOI: 10.1002/aenm.202303367

cells used upright device structures grown on InP and were left on substrate, with a reflector placed behind the substrate.[15,19] Inverted growth enables direct access to the rear surface of the device, which permits the application of high reflectivity metals or dielectrics while removing the necessity to use semi-insulating substrates with the attendant processing complexities.[15] Inverted growth is also compatible with epitaxial liftoff techniques, which enable removal of the device from the substrate.[20] The device can be placed on a flexible handle and/or heat sink, and the substrate can potentially be reused to save cost. Furthermore, the graded buffer can be removed[17] to reduce sub-bandgap absorption, which is another critical parameter affecting TPV efficiency.[11] Alternatively, the graded buffer could be left in the device to improve current spreading in high-power LPCs.

Growth of these devices on a substrate other than InP, such as GaAs, is desirable for the following reasons. InP is generally available in diameters up to 100 mm, whereas GaAs is available in sizes up to 200 mm, making GaAs more scalable at the high volumes needed for applications such as thermal grid storage. GaAs costs significantly less than InP on an areal basis, and we estimate that a 0.6 eV metamorphic GaInAs cell grown on GaAs would be 4–5x less expensive than one grown on InP even considering the added cost of the additional metamorphic grading.[21] Another advantage is that GaAs is considerably less brittle than InP, which potentially reduces yield losses due to breakage. Lastly, we note that GaAs has nearly the same lattice constant as Ge substrates, meaning that any device recipes developed on GaAs would be generally compatible with Ge substrates, which are available up to 300 mm diameter.[22] These factors are significant drivers of manufacturability and cost reduction, if devices grown on GaAs achieve sufficiently high performance.

In this work, we study the inverted metamorphic growth of 0.58–0.59 eV $Ga_{0.30}In_{0.70}As$ photovoltaic cells on InP and GaAs substrates employing broadband rear reflectors. We evaluate the effect of the different lattice mismatch, 1.2% on InP substrates versus 5.0% on GaAs substrates, on the defect structure of the graded buffers used to bridge the lattice constant gap between the substrate and device layers. We compare the performance of these devices under high irradiance and use these high-intensity data to estimate their TPV efficiency, $\eta_{TPV,}$ as a function of black body emitter temperature and discuss a path to $\eta_{TPV} > 24\%$ at 1100 °C. Lastly, we estimate their LPC efficiency, $\eta_{LPC,}$ using an idealized 2.0 µm emitter.

2. Results and Discussion

2.1. Structural Characterization

Figure 1 shows device structures for the ≈0.58–0.59 eV $Ga_{0.30}In_{0.70}As$ devices grown on InP and GaAs substrates. The $Ga_{0.30}In_{0.70}As$ pn junction where the carrier collection occurs is identical in both devices, but the device on GaAs utilizes a thicker compositionally graded buffer to bridge the significantly larger lattice mismatch (5.0%, versus 1.2% on InP). The first portion of that graded buffer utilizes the $Ga_xIn_{1-x}P$ alloy from $Ga_{0.5}In_{0.5}P$ to InP, and then the buffer switches to an InP_yAs_{1-y} alloy for the remainder of the grading. The InP-based device only uses the InP_yAs_{1-y} portion of the graded buffer. See the Experimental Section below for complete growth details.

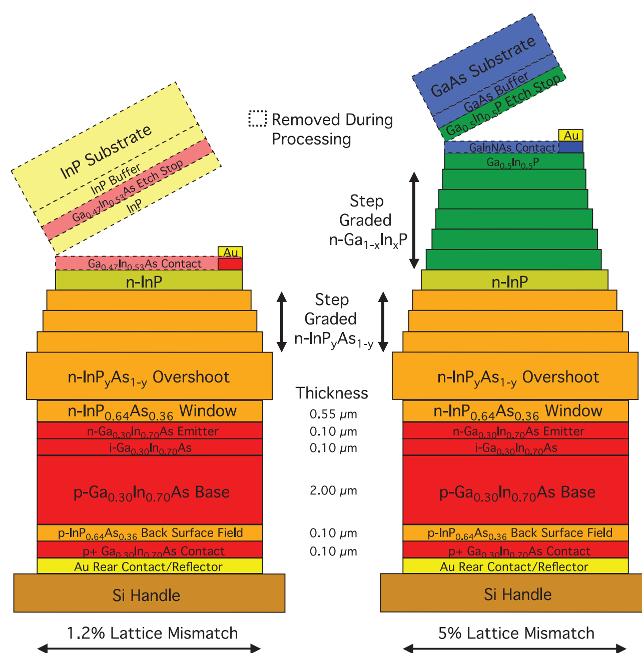

Figure 1. Structure of devices grown on InP and GaAs. The width of the layers indicates the relative lattice constant, i.e., wider layers have a larger lattice constant, and layers with different widths are lattice-mismatched. Color roughly indicates relative bandgap. There are more steps in the actual graded buffers than depicted here. The growth direction is from top to bottom.

First, we characterized the surface defect structure of the two types of graded buffers. **Figure 2** shows atomic force microscopy (AFM) images, plan view scanning electron microscopy (SEM) images, and panchromatic cathodoluminescence (CL) images for InP-based [(a)-(c)] and GaAs-based [(d)-(f)] compositional grades. Both grades exhibit cross-hatched surfaces, characteristic of mismatched epitaxy using graded buffers. The GaAs based grade is significantly rougher, with a root mean square (RMS) roughness of 44.6 nm in a 70 × 70 µm square scan versus 18.5 nm for the graded buffer grown on InP. We note that the near-normal reflectance of the surface measured by an in situ optical tool decreased significantly during the growth of the InP_yAs_{1-y} portion of that sample, implying that most of the roughening occurred during the growth of those layers (see Figure S1, Supporting Information for reflectance data). The surface of compositionally graded buffers roughens in response to inhomogeneous strain fields created by dislocations,[23,24] and In is known to have a relatively high surface diffusion rate compared to other adatoms such as Ga or Al,[24,25] making it more likely to cause roughening. Furthermore, surface roughening in metamorphic epitaxy exhibits hysteresis, meaning that prior accumulation (or removal) of roughness impacts the roughness of subsequent growth.[26,27] Thus, the growth of this strained, In-rich layer, after the prior deposition of a grade from GaAs to InP created a situation where the surface was highly susceptible to roughening. The InP_yAs_{1-y} grade grown directly on the InP substrate

© 2024 The Authors. Advanced Energy Materials published by Wiley-VCH GmbH

16146840, 2024, 10, Downloaded from https://onlinelibrary.wiley.com/doi/10.1002/aenm.202303367 by National Renewable Energy Lab Charity Harada, Wiley Online Library on [07/03/2024]. See the Terms and Conditions (https://onlinelibrary.wiley.com/terms-and-conditions) on Wiley Online Library for rules of use; OA articles are governed by the applicable Creative Commons License

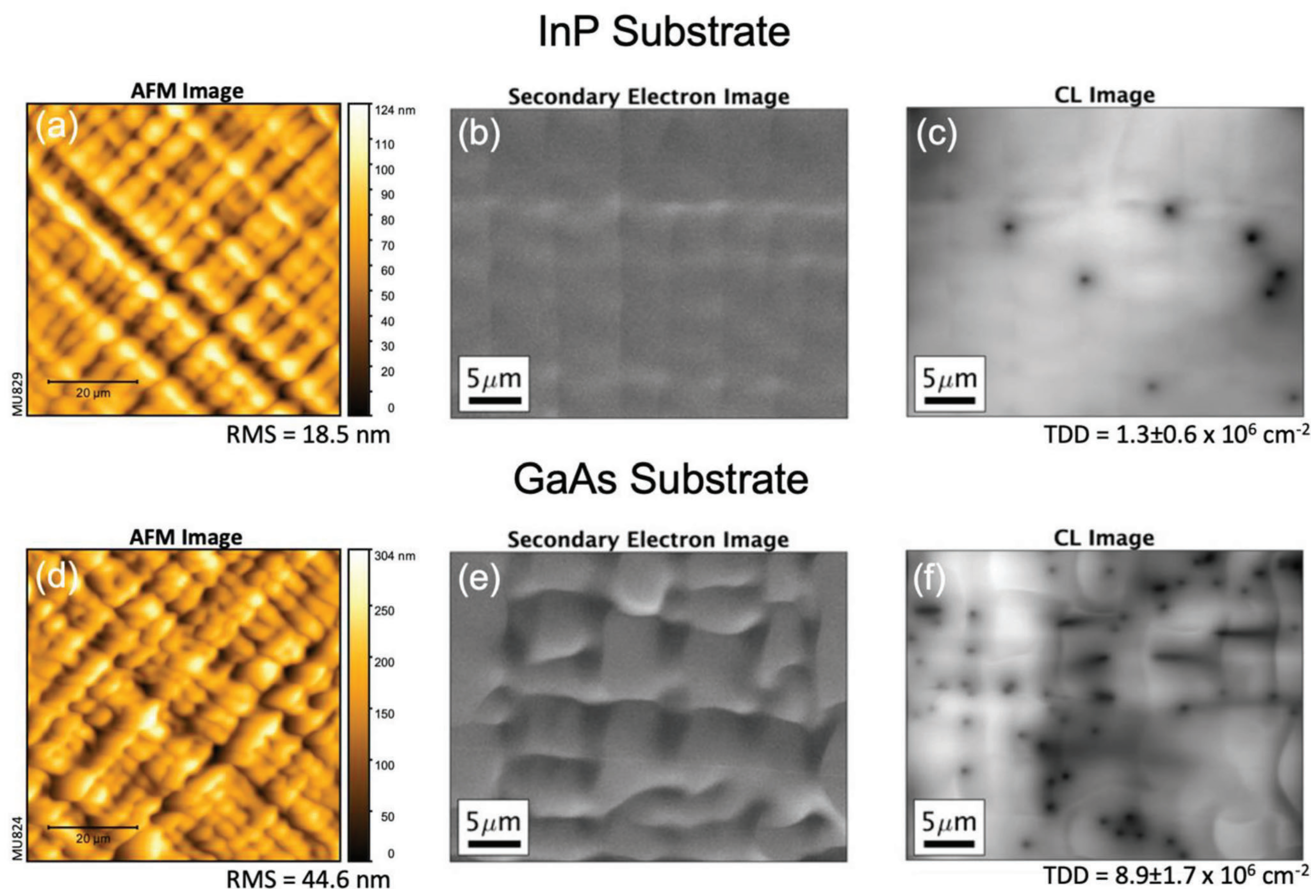

Figure 2. Atomic force microscopy (AFM), scanning electron microscopy (SEM), and cathodoluminescence (CL) images for graded buffers to the Ga0.30In0.70As lattice constant based on InP [(a)-(c)] and GaAs [(d)-(f)] substrates. The SEM and CL images are taken from the exact same place. The root mean square (RMS) roughness is listed below each AFM image. The threading dislocation density, averaged over a series of 8 images from each sample, is listed below each CL image. The error bar presented is one standard deviation from the mean value.

does not roughen as dramatically because of the pristine starting surface. Looking at the CL images, Figure 2c,f, the InP-based grade exhibits a threading dislocation density (TDD) of $1.3 \pm 0.6 \times 10^6$ cm^{-2} which compares quite favorably to TDD reported in similar graded buffers.[28] The TDD is almost an order of magnitude higher in the GaAs based grade, with TDD = $8.9 \pm 1.7 \times 10^6$ cm^{-2}. This is ≈2–3× higher than we observe in GaInP grades from GaAs to InP,[29] suggesting that TDD increase occurred during growth of the InP_yAs_{1-y} portion of the grade between InP and final lattice constant. Surface roughness correlates with higher TDD,[30,31] either by actively creating drag on gliding dislocations, reducing the amount of strain relaxation per TD, or as a sign of the presence of compositional variation (phase separation) which also restricts glide.[32,33] Given that phase separation is not usually observed[28] in InP_yAs_{1-y}, it is likely that the increased roughening that occurred during the grade of the GaAs-based sample reduced the velocity of gliding dislocations, increasing their density. Comparing the SEM and CL images in panels 2e,f, it appears that the TD spots are concentrated in the troughs in the rough surface, suggesting that they have been trapped there due to the roughness. Managing this roughening behavior will be key to reducing TDD in these grades in the future.

2.2. Device Measurements

Next, we studied the behavior of the $Ga_{0.30}In_{0.70}As$ devices under the one-sun AM1.5G reference spectrum and irradiance to benchmark their performance. **Figure 3a** shows the external and internal quantum efficiency (EQE and IQE) and Figure 3b shows light current density-voltage (J--V) curves, respectively, for these devices. The data presented are for champion devices out of 11 devices fabricated from each growth, although we note that the performance did not vary much across these devices (see Figure S2, Supporting Information, for data on all devices). The short wavelength cutoff in the QE results from absorption in the graded buffer. The bandgaps of these devices vary slightly, possibly due to reactor drift, variance in In/Ga incorporation efficiency on surfaces with varying roughness, or residual strain differences. Both devices show a high degree of carrier collection with peak IQE of ≈97% for both devices. The open circuit voltage (V_{OC}) at one-sun is 45 mV larger in the InP-based device relative to the GaAs-based device, 0.200 versus 0.155 V, which we attribute to the significantly lower TDD achieved on InP. The bandgap voltage offsets ($W_{OC} = E_G/q - V_{OC}$) at this irradiance are 0.38 and 0.44 V for InP- and GaAs-based devices, respectively. The fill factors (FFs) for these cells are 61.5% and 54.5%, respectively.

© 2024 The Authors. Advanced Energy Materials published by Wiley-VCH GmbH

16146840, 2024, 10, Downloaded from https://onlinelibrary.wiley.com/doi/10.1002/aenm.202303367 by National Renewable Energy Lab Charity Harada, Wiley Online Library on [07/03/2024]. See the Terms and Conditions (https://onlinelibrary.wiley.com/terms-and-conditions) on Wiley Online Library for rules of use; OA articles are governed by the applicable Creative Commons License

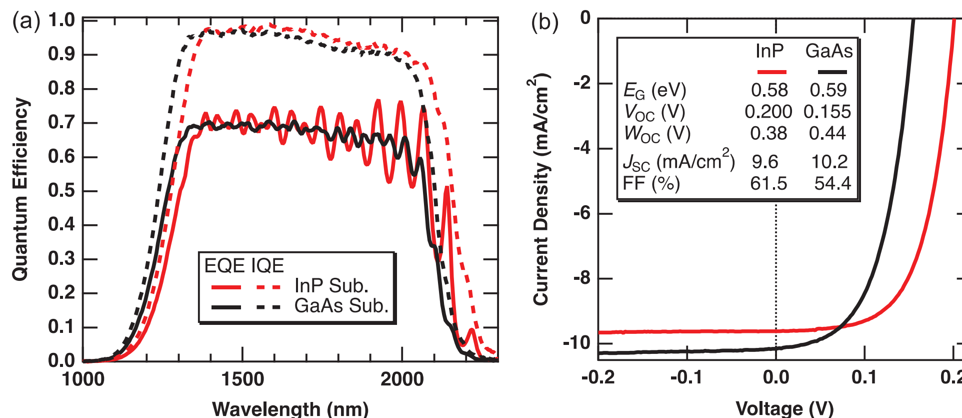

Figure 3. Quantum efficiency (a) and light *J–V* curves under a one-sun spectrum (b) for the devices based on InP and GaAs.

We then characterized these devices under high irradiance using a high-intensity pulsed solar simulator (HIPSS), to assess their performance under irradiance levels similar to TPV or laser power conversion applications. These measurements provide the dependence of V_{OC} and FF on irradiance, as tracked by the J_{SC}. As described below, we then use the EQE to map J_{SC} and thus also V_{OC} and FF onto the TPV spectrum of interest, effectively using the cell as its own reference cell to correct for the spectral mismatch between the spectrum of the simulator and spectrum of interest. The HIPSS irradiance was varied up to 45 W cm^{-2} using an aperture. See Figure S3 (Supporting Information) for more details about the HIPSS spectrum and how it maps to idealized blackbody spectra of varying temperature. **Figure 4**a shows select light *J–V* curves, (b) shows V_{OC}, FF, and equivalent

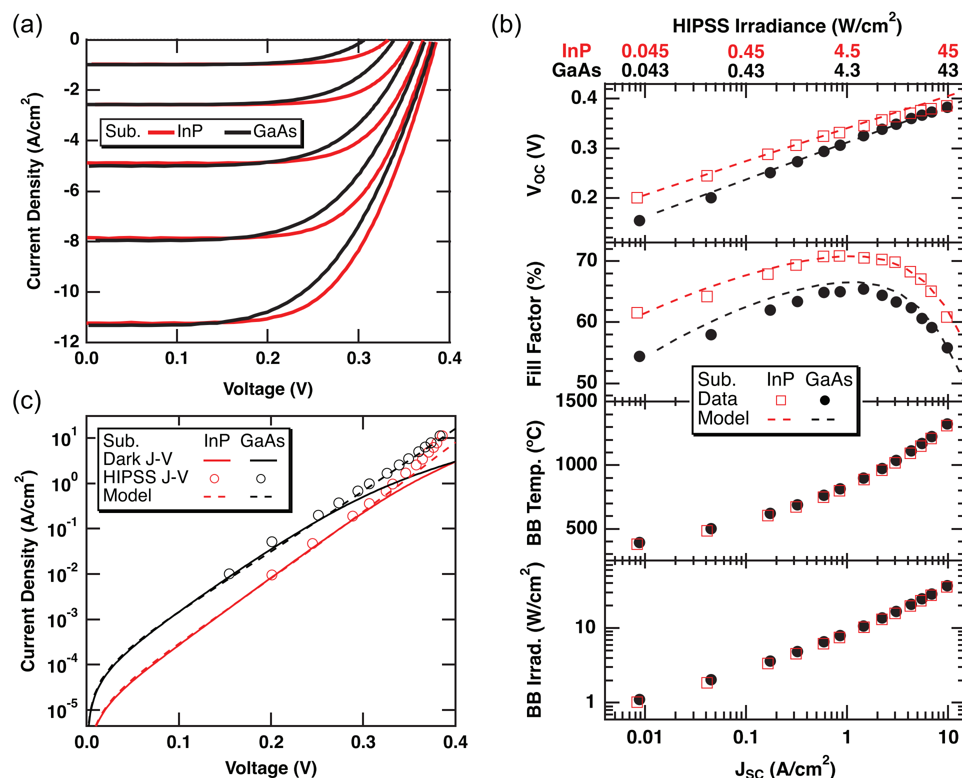

Figure 4. a) High-intensity light *J–V* curves measured on the <0.6 eV devices grown on InP and GaAs using a solar simulator with a pulsed Xe arc lamp and GaAs filter. The light intensity was adjusted by varying the width of an aperture in front of the lamp. b) V_{OC}, fill factor (FF), equivalent blackbody (BB) temperature, and equivalent blackbody irradiance as a function of J_{SC} for these high-intensity measurements. The irradiance of the high-intensity pulsed solar simulator (HIPSS) tool used for these measurements that corresponds to the measured J_{SC} is indicated for each device on the mirror *x*-axis. For a given J_{SC}, the lower two panels plot the blackbody temperature and irradiance that would generate an equivalent J_{SC} in the device (see Figure S3, Supporting Information, for more detail about this calculation). c) Dark *J-V* curves of the two devices. The J_{SC}–V_{OC} pairs from (b) are plotted on the graph as open circles to show device behavior unaffected by series resistivity. Fits to a two-diode device model are plotted as broken lines in (b) and (c).

© 2024 The Authors. Advanced Energy Materials published by Wiley-VCH GmbH

16146840, 2024, 10, Downloaded from https://onlinelibrary.wiley.com/doi/10.1002/aenm.202303367 by National Renewable Energy Lab Charity Harada, Wiley Online Library on [07/03/2024]. See the Terms and Conditions (https://onlinelibrary.wiley.com/terms-and-conditions) on Wiley Online Library for rules of use; OA articles are governed by the applicable Creative Commons License

Table 1. Fit parameters for the device model.

	InP-based	GaAs-based
J_{01} [A cm^{-2}]	8.4×10^{-07}	7.3×10^{-07}
J_{0n} [A cm^{-2}]	1.1×10^{-05}	7.5×10^{-05}
n	1.3	1.3
R_S [mΩ cm^2]	6.9	8.5

blackbody temperature and irradiance (see figure caption) versus J_{SC}, and (c) shows dark J–V curves for both devices. The V_{OC}–J_{SC} pairs from (b) are placed as open circles on the dark J–V curves in (c), to show the device behavior at high current density in absence of series resistance, which does not affect the V_{OC} determination because no current is flowing at that voltage. We fit the dark J–V and HIPSS data to a double-diode optoelectronic device model[34] to derive more understanding from the data. The fits are shown as broken lines in panels (b) and (c), and the fit parameters are shown in **Table 1**, where J_{01} is the diode saturation current for the diode representing recombination in the quasi-neutral regions, J_{0n} is the diode saturation current for the diode representing recombination in the space charge region, n is the diode ideality factor, and R_S is the series resistivity. Initially, the V_{OC} of the InP-based device increases logarithmically with J_{SC}, but then begins to deviate from the model fit, likely due to device heating that occurs at higher irradiances. We measure a V_{OC} of 0.386 V (W_{OC} = 0.20 V) under the highest irradiance tested, which yielded a J_{SC} of 10 A cm^{-2}. The current generated by this HIPSS irradiance is the same as would be generated by a ≈1300 °C blackbody, which has an irradiance of ≈36 W cm^{-2}. The model suggests that the V_{OC} would be 0.401 V (W_{OC} = 0.18 V) at this irradiance if not for the device heating. The FF peaks at 70.8% when the J_{SC} is 0.9 A cm^{-2}, and the product V_{OC}FF peaks when the J_{SC} is 3.0 A cm^{-2}, above which point the series resistance from the contacts causes significant reductions in FF.

The performance of the GaAs-based device is reduced compared to the InP-based device because the J_{0n} current is over 7× larger. We attribute this change to increased nonradiative recombination at dislocations, because the GaAs-based device has a larger TDD and the devices have roughly equal J_{01} (in fact, the GaAs-based cell has slightly lower J_{01} because its bandgap is slightly larger). The V_{OC} of the GaAs-based device therefore increases faster with current density relative to the InP-based device. We fit the ideality factor of the J_{0n} diode in both devices as 1.3, which is somewhat lower than commonly observed but within the expected range.[35] Devices utilizing compositionally graded buffers that are limited by recombination at dislocations at low current density often show a J_{0n} ideality factor of $1 < n < 2$. We have previously observed $n = 1.5$ in our metamorphic GaInAs junctions.[36] This reduced ideality factor means that the V_{OC} versus J_{SC} curves do not converge in the current density range tested despite the similar J_{01} parameters. We measure a V_{OC} of 0.383 V (W_{OC} = 0.21 V) at an irradiance corresponding to J_{SC} = 9.8 A cm^{-2}, while the FF peaks at 65.4% when the J_{SC} = 1.5 A cm^{-2}. The V_{OC}FF product peaks when J_{SC} = 4.3 A cm^{-2} with V_{OC} = 0.360 V and FF = 62.4%. V_{OC}FF peaks at higher J_{SC} for this device compared to the one on InP even though the series resistance was slightly higher. We attribute this fact to reduced heating in the GaAs based device, which is indicated by minimal deviation of the HIPSS V_{OC} data from the best fit in Figure 4c. Thus the penalty that heating places on V_{OC} and FF is reduced. One possible reason that the device temperature is lower is the additional device thickness of the grade from GaAs to InP, which adds ≈5 µm of thickness on top of the ≈7 µm combined from the InP_yAs_{1-y} graded buffer and GaInAs device layer thickness in the InP-based device. This extra thickness could aid with heat dissipation in the device during the pulsed measurement. We note that we had considered Auger recombination, which can affect low bandgap III-V devices,[37] as a cause of the V_{OC} droop at high current density observed in the InP-based device, but the absence of droop at high current density in the GaAs-based device suggests that heating was indeed the cause. Variations in the thickness of the epoxy that bonds the device to the Si handle could also explain the varied device heating (see Experimental Section).

The device metrics obtained here are comparable to other cells with similar bandgaps of ≈0.6 eV.[19,38] A recent summary of device results is provided in Gamel et al.[39] Notably, Cederberg et al. reported a V_{OC} of 0.348 V junction^{-1} in a 0.6 eV InP-based five-junction GaInAs monolithic interconnected module (MIM) with a J_{SC} of 1.7 A cm^{-2}. The cell was measured under an infrared lamp. This device, or a similar one from that group yielded 0.377 V under a spectrally selective emitter. Su et al. reported a voltage of 0.37 V with a J_{SC} of ≈1 A cm^{-2} measured under a solar simulator in a ≈0.6 eV GaInAs device. The bandedge in the QE for that cell suggests a bandgap of ≈0.61–0.62 eV. The InP- and GaAs-based cells presented in this work exhibit V_{OC} = 0.346 and 0.325 V with J_{SC} of ≈1.5 A cm^{-2}. These voltages are slightly lower, but the differences correspond with slightly smaller bandgaps by 0.02–0.04 eV. These devices are grown inverted and lifted off the substrate, whereas previous devices in the literature were grown upright and left on wafer.

2.3. Thermophotovoltaic Efficiency Modeling

Next, we used the high-intensity J–V measurements combined with measurements of the spectral reflectance of the devices to estimate TPV efficiency as a function of blackbody temperature. **Figure 5a** shows the normal reflectance as a function of wavelength on the left axis, with blackbody spectra at various temperatures overlaid on the right axis for reference. We did not measure the angular dependence of the reflectance, but note that near-normal measurements are generally a good predictor of results using analytical angle-integrated calculations.[40] Above bandgap, the reflectance is ≈0.3 for both cells, typical of III-V cells without antireflection coating. The sub-bandgap reflectance is significantly higher in the InP-based device compared to the GaAs-based device. This difference implies that there is more sub-bandgap absorption in the GaAs-based device, which we suspect occurs in its thicker graded buffer, because the remainder of the structure is nominally identical. The absorption mechanism is likely a combination of free carrier absorption and absorption caused by dislocations.[41,42] Given that the lattice mismatch between the substrate and device is much larger on GaAs (1.2% versus 5%) the graded buffer on GaAs contains a considerably larger volume of dislocations (both threads and misfit

© 2024 The Authors. Advanced Energy Materials published by Wiley-VCH GmbH

16146840, 2024, 10, Downloaded from https://onlinelibrary.wiley.com/doi/10.1002/aenm.202303367 by National Renewable Energy Lab Charity Harada, Wiley Online Library on [07/03/2024]. See the Terms and Conditions (https://onlinelibrary.wiley.com/terms-and-conditions) on Wiley Online Library for rules of use; OA articles are governed by the applicable Creative Commons License

16146840, 2024, 10, Downloaded from https://onlinelibrary.wiley.com/doi/10.1002/aenm.202303367 by National Renewable Energy Lab Charity Harada, Wiley Online Library on [07/03/2024]. See the Terms and Conditions (https://onlinelibrary.wiley.com/terms-and-conditions) on Wiley Online Library for rules of use; OA articles are governed by the applicable Creative Commons License

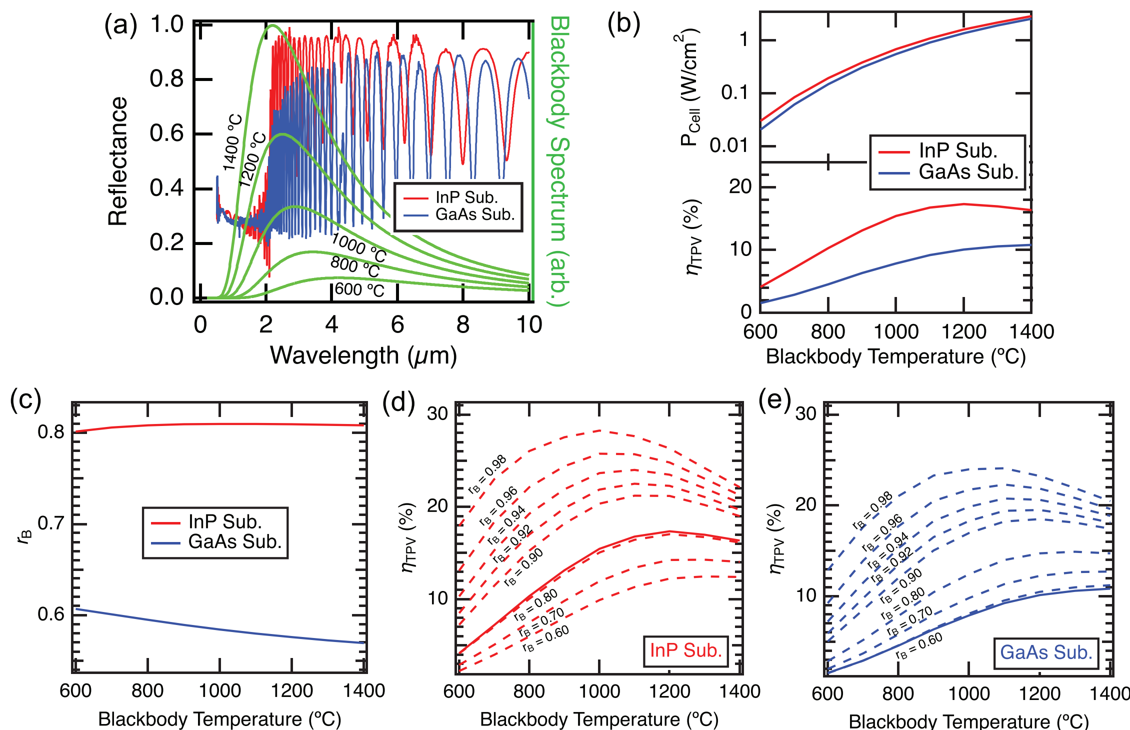

Figure 5. Thermophotovoltaic (TPV) efficiency estimates. a) Spectral reflectance of the <0.6 eV devices grown on InP and GaAs substrates. The blackbody spectra at various temperatures are plotted as green curves on the right axis. b) Power produced by the cells (top) and η_{TPV} (bottom) plotted as a function of blackbody temperature. c) Power-weighted sub-bandgap reflectance (r_B) for each cell as a function of blackbody temperature. d,e) TPV efficiency versus blackbody temperature at multiple values of r_B for the cell grown on the InP or the GaAs substrate. The curves from panel (b) are overlaid as solid lines in (d) and (e).

dislocations) which may contribute to increased sub-bandgap absorption in this device.

Next we estimate η_{TPV} as a function of blackbody temperature. The blackbody radiation spectrum is calculated using Planck's law. We use the equation:

$$\eta_{TPV} = \frac{P_{cell}}{P_I - P_R} \tag{1}$$

where $P_{cell} = V_{OC}J_{SC}FF$ is the power generated by the cell, P_I is the power incident on the cell at a given blackbody temperature assuming unity view factor, and P_R is the power reflected by the cell back to the hypothetical emitter. P_R is not counted as a loss because the energy is reabsorbed and then reradiated by the emitter.[17] P_{cell} is estimated by first integrating the EQE of the cells with the blackbody spectrum to get J_{SC}, and then determining V_{OC} and FF at that J_{SC} by interpolating the data in Figure 4b. See Figure 4b and Figure S3c (Supporting Information) for information about how the flash measurements map to a measurement under a blackbody emitter. P_R is determined by integrating the reflectance with the blackbody spectrum. Figure 5b plots P_{cell} and η_{TPV} as a function of blackbody temperature. The cell grown on InP provides more power at a given temperature because of its superior device metrics. As one point of comparison, the InP cell yields 1.09 W cm^{-2} at 1100 °C, 18.4% more power than the 0.92 W cm^{-2} provided by the GaAs cell. While this difference is reasonable given the increased TDD in the GaAs cell, η_{TPV} for the InP cell is 83% higher relative to the GaAs efficiency (16.8% versus 9.2%), due to the large penalty paid to the high sub-bandgap absorption in the GaAs-based cell. The peak efficiency for the InP-based cell is 17.4% at 1200 °C versus 10.8% at 1400 °C for the GaAs cell. We note that application of an antireflection coating to these devices would increase these efficiencies by reducing the sub-bandgap absorption loss by ensuring more of the high energy photons are absorbed and converted on the first pass.

Improvement of the sub-bandgap reflectance is another promising route to improve the TPV efficiency of both devices. The power-weighted sub-bandgap reflectances (r_B) for the InP and GaAs-based cells hover around ≈80% and ≈60%, respectively, as shown in Figure 5c. We modeled the effect of r_B on η_{TPV} as a function of blackbody temperature for each cell as shown in Figure 5d,e. η_{TPV} increases strongly with r_B for both cells by reducing the value of the denominator in Equation (1). We expect that removal of the graded buffer would significantly increase r_B in these cells. Previously we demonstrated $r_B = 0.931$ in an inverted metamorphic tandem device at the $Ga_{0.70}In_{0.30}As$ lattice constant that had the graded buffer removed.[17] Integration of the reflectance from that cell with the 1000 °C blackbody temperature yields $r_B = 0.935$, providing a reasonable target for the present cells if a similar, removable graded buffer can be developed. If we achieve this value in an optimized device design that removes the grade, the efficiency of the InP and GaAs cells would peak at ≈1100 °C at values of 24.0% and 20.7%, respectively. Devices using more sophisticated reflector designs such as an air

© 2024 The Authors. Advanced Energy Materials published by Wiley-VCH GmbH

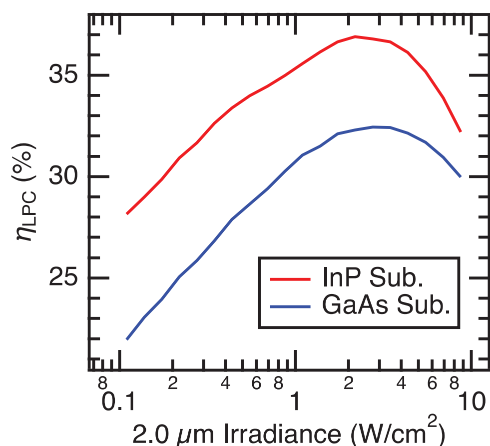

Figure 6. Estimated laser power conversion efficiency as a function of monochromatic irradiance from a hypothetical 2.0 μm laser source.

gap have demonstrated r_B up to 0.985,[18] implying even higher efficiencies are possible if those architectures could be incorporated in an optimized device.

2.4. Laser Power Conversion Efficiency Modeling

Another application for these devices is laser power conversion in the 2.0–2.3 μm atmospheric window. In this section, we estimate a laser power conversion efficiency assuming an EQE of 0.9 at 2 μm with a properly tuned antireflection coating [see IQE in Figure 3a]. Assuming a variable, monochromatic power source with a wavelength of 2.0 μm, we can calculate J_{SC} from the following equation:[43,44]

$$J_{SC} = E_{tot} \mathrm{EQE}(\lambda) \left(\frac{hc}{q\lambda}\right)^{-1} \tag{2}$$

where E_{tot} is the total irradiance in W cm^{-2} and $\frac{hc}{q\lambda} = 0.62$ eV for $\lambda = 2.0$ μm. The laser power conversion efficiency is then calculated by:

$$\eta_{LPC} = \frac{P_{Cell}}{E_{tot}} \tag{3}$$

where P_{Cell} is determined as a function of J_{SC} from the flash measurements as described above for the TPV estimate. **Figure 6** plots η_{LPC} as a function of 2.0 μm irradiance.

The device grown on the InP substrate yields an estimated peak efficiency of 36.8% under an irradiance of 1.86 W cm^{-2}. The GaAs efficiency peaks at a higher current density presumably due to improved heat dissipation, yielding a 32.5% conversion efficiency at 2.81 W cm^{-2}. We note that use of multijunction devices could yield significant improvements by reducing series resistance losses.

3. Conclusion

We developed inverted metamorphic $Ga_{0.3}In_{0.7}As$ photovoltaic converters with bandgaps below 0.60 eV grown on InP and GaAs substrates. These devices have application as TPV or converters for laser power beaming in the 2.0–2.3 μm atmospheric window. The device grown on GaAs exhibits a higher TDD, yet the devices yield comparable V_{OC}s under high irradiance. The GaAs-based device has a lower sub-bandgap reflectance than the InP-based device, which we attribute to absorption in the thicker graded buffer in that device. We estimate the InP- and GaAs-based devices to yield 1.09 W cm^{-2} versus 0.92 W cm^{-2}, respectively, under a 1100 °C blackbody, with TPV efficiencies of 16.8 versus 9.2%. Removal of the graded buffers from these devices would lead to significant increases in sub-bandgap reflectance and TPV efficiency. We estimate that the efficiencies would peak at ≈1100 °C at values of 24.0% and 20.7% with reflectances previously achieved in other metamorphic devices with removed graded buffers. As LPCs, we estimated peak efficiencies of 36.8% and 32.5% under irradiation from an idealized 2.0 μm source.

4. Experimental Section

All devices were grown by organometallic vapor phase epitaxy (OMVPE) using standard precursors. The wafer curvature and surface reflectivity were monitored in situ using a multibeam optical stress sensor (see Figure S1, Supporting Information). Substrates were either (100) InP:S or (100) GaAs:Si with a misorientation of 2° toward the (111)B plane. The device structures were shown in Figure 1. The device on InP was grown with a InP:Si buffer, a 1 μm $Ga_{0.47}In_{0.53}As$:Si etch stop layer followed by a 0.5 μm InP:Si second etch stop layer, then a 0.2 μm $Ga_{0.47}In_{0.53}As$:Se front contact layer, where the element listed after the colon indicates the dopant. Next a InP_xAs_{1-x}:Si step–graded buffer was grown with 0.5 μm steps and a strain grading rate of 0.33% strain μm^{-1}. The strain overshoot layer of the grade was grown 1.0 μm thick, and then the device layers were grown lattice-matched to the in-plane lattice constant of the overshoot. The total lattice mismatch between the device layers and the substrate is 1.2%. The front junction $Ga_{0.30}In_{0.70}As$ device layers and thicknesses are listed in Figure 1. The emitter doping density was nominally 1×10^{18} cm^{-3} Se, while the Zn doping density in the base was measured by the capacitance-voltage method to be 2×10^{16} and 5×10^{16} cm^{-3} in the devices grown on GaAs and InP, respectively, despite the molar fraction of dimethylzinc dopant being equal during each growth. It is likely that dopant incorporation rates are slightly different in each device due to differences in surface roughness. $InP_{0.64}As_{0.36}$ doped $\approx 1 \times 10^{18}$ cm^{-3} with Si or Zn was used to passivate the front and rear surfaces of the device, respectively. The device grown on GaAs substrate used a $Ga_{0.5}In_{0.5}P$:Se etch stop and GaInNAs:Se[45] front contact layer, followed by a $Ga_xIn_{1-x}P$:Si graded buffer from GaAs to InP, and then the same InP_xAs_{1-x}:Si graded buffer used in the cell grown on InP. The $Ga_xIn_{1-x}P$ buffer was graded in 0.25 μm steps at 1% strain μm^{-1} from $x_{Ga} = 0.50$–0.20, and then 0.5% strain μm^{-1} from $x_{Ga} = 0.20$–0.00 (InP) using 0.125 μm steps.[46] The total lattice mismatch from substrate to device is 5.0%. For both devices, the growth temperature and V/III ratios for the $Ga_xIn_{1-x}P$ grade, $In_xP_{1-x}As$ grade, and $Ga_{0.30}In_{0.70}As$ cell were 675 °C and 560, 660 °C and 780, and 620 °C and 130, respectively. The dislocation density of the graded buffers was analyzed by CL in a scanning electron microscope. Panchromatic CL intensity images were collected using a parabolic mirror to direct the emission due to radiative transitions to a liquid nitrogen cooled Ge photodiode. An accelerating voltage of 15 kV and electron beam current of ≈0.7 nA were used to generate excess carriers in the samples. Separate structures for CL analysis were grown that stopped at the $InP_{0.64}As_{0.36}$ layer, which had a bandgap (E_G) of 0.93 eV, because the cooled Ge CL detector ($E_G = 0.66$ at room temperature) could not detect emission from $Ga_{0.30}In_{0.70}As$. It was assumed that the TDD measured in the final grade layer was roughly the same as that in the $Ga_{0.30}In_{0.70}As$ device layers, which were grown lattice-matched to the in-plane lattice constant of the graded buffer.

© 2024 The Authors. Advanced Energy Materials published by Wiley-VCH GmbH

16146840, 2024, 10, Downloaded from https://onlinelibrary.wiley.com/doi/10.1002/aenm.202303367 by National Renewable Energy Lab Charity Harada, Wiley Online Library on [07/03/2024]. See the Terms and Conditions (https://onlinelibrary.wiley.com/terms-and-conditions) on Wiley Online Library for rules of use; OA articles are governed by the applicable Creative Commons License

After growth, devices were made by first electroplating the Au rear contact, which also serves as the rear reflector, and then bonding that contact to a Si substrate handle with a low viscosity epoxy. The epoxy thickness was estimated to be 10–15 µm based on previous experience. Next, the substrate was removed using wet chemical etchants that did not react with the etch stop layers. Then the front contact concentrator grid was defined by photolithography and electroplated onto the front contact layer. Square 0.116 cm^2 devices were defined by photolithography and mesas were isolated using selective wet etching.[47] The wavelength-dependent EQE was measured on a calibrated system with 2600 nm GaInAs reference diode and a second 2600 nm diode to concurrently collect specular reflectance at a ≈15° angle from the sample surface normal. IQE was calculated from EQE and the wavelength-dependent reflectance, $r(\lambda)$ using the equation $\mathrm{IQE}(\lambda) = \mathrm{EQE}(\lambda)/[1 - r(\lambda)]$. *J-V* was measured in the dark and in the light at 25 °C under an XT-10 system with a Xe arc lamp. Due to the lack of a calibrated reference cell with the same bandgap as the cell, the cell was used as its own reference, adjusting the distance between the lamp and the cell until the measured J_{SC} matched that calculated by integration of the EQE with the ASTM G173 AM1.5 Global spectrum. Based on comparisons between EQE and *J-V* measurements for higher bandgap single-junction cells for which we have good reference cells, the systematic uncertainty was estimated to be <3%. We note that AM1.5G is not an appropriate reference spectrum for TPV and LPC applications, but it was useful as a well-defined reference. The devices were characterized under high intensity irradiation using a HIPSS with a Xe arc lamp and a GaAs filter to eliminate radiation below 880 nm. The approximate spectrum is shown in ref. [17]. The irradiance was controlled by varying the size of an aperture in front of the lamp.

The reflectance was measured in a normal configuration using a Bruker V70 Fourier-transform infrared (FTIR) spectrometer and a Hyperion 2000 microscope. An aperture of spot size approximately 0.01 mm^2 was used and the spot was placed completely between the front contract gridlines of the device. The three spectral ranges come from three different combinations of light sources/beam splitters/detectors with the visible range coming from tungsten lamp/Quartz beam splitter/Silicon detector, the Near IR from Tungsten lamp/Quartz beam splitter/HgCdTe detector, and the Mid IR coming from Globar/KBr beam splitter/ HgCdTe detector. All measurements were taken at room temperature and referenced to a NIST standard that has known reflectance to within +/−0.4% absolute.

Supporting Information

Supporting Information is available from the Wiley Online Library or from the author.

Acknowledgements

The authors would like to thank Michelle Young for device growth and Sarah Collins for device processing. This work was authored by the National Renewable Energy Laboratory (NREL), operated by Alliance for Sustainable Energy, LLC, for the U.S. Department of Energy (DOE) under Contract No. DE-AC36-08GO28308. This work was supported by the Laboratory Directed Research and Development (LDRD) Program at NREL. Support for E.J.T. and T.D. was provided by the University of Wisconsin-Madison, Office of the Vice Chancellor for Research and Graduate Education with funding from the Wisconsin Alumni Research Foundation. The views expressed in the article do not necessarily represent the views of the DOE or the U.S. Government. The U.S. Government retains and the publisher, by accepting the article for publication, acknowledges that the U.S. Government retains a nonexclusive, paid-up, irrevocable, worldwide license to publish or reproduce the published form of this work, or allow others to do so, for U.S. Government purposes.

Conflict of Interest

The authors declare no conflict of interest.

Data Availability Statement

The data that support the findings of this study are available from the corresponding author upon reasonable request.

Keywords

III-V photovoltaics, inverted metamorphic solar cell, laser power conversion, organometallic vapor phase epitaxy, thermophotovoltaics

Received: October 6, 2023
Revised: December 1, 2023
Published online: January 19, 2024

[1] A. Datas, A. Ramos, A. Martí, C. Del Cañizo, A. Luque, *Energy* **2016**, *107*, 542.
[2] Z. Utlu, U. Parali, Ç. Gültekin, *Energy Technol.* **2018**, *6*, 1039.
[3] H. Jouhara, N. Khordehgah, S. Almahmoud, B. Delpech, A. Chauhan, S. A. Tassou, *Therm. Sci. Eng. Prog.* **2018**, *6*, 268.
[4] N. Kaffezakis, S. Terlizzi, C. Smith, A. S. Erickson, S. K. Yee, D. Kotlyar, *Ann. Nucl. Energy* **2020**, *141*, 107311.
[5] A. Datas, A. Martí, *Sol. Energy Mater. Sol. Cells* **2017**, *161*, 285.
[6] C. Amy, H. R. Seyf, M. A. Steiner, D. J. Friedman, A. Henry, *Energy Environ. Sci.* **2019**, *12*, 334.
[7] C. Algora, I. García, M. Delgado, R. Peña, C. Vázquez, M. Hinojosa, I. Rey-Stolle, *Joule* **2022**, *6*, 340.
[8] K. Scholle, S. Lamrini, P. Koopmann, P. Fuhrberg, in *Frontiers in Guided Wave Optics and Optoelectronics*, IntechOpen, London, UK **2010**.
[9] T. Burger, C. Sempere, B. Roy-Layinde, A. Lenert, *Joule* **2020**, *4*, 1660.
[10] C. Wang, presented at *AIP Conference Proceedings*, **2004**.
[11] E. J. Tervo, R. M. France, D. J. Friedman, M. K. Arulanandam, R. R. King, T. C. Narayan, C. Luciano, D. P. Nizamian, B. A. Johnson, A. R. Young, L. Y. Kuritzky, E. E. Perl, M. Limpinsel, B. M. Kayes, A. J. Ponec, D. M. Bierman, J. A. Briggs, M. A. Steiner, *Joule* **2022**, *6*, 2566.
[12] R. Wehrer, M. Wanlass, D. Taylor, B. Wernsman, J. Carapella, R. Schultz, S. Ahrenkiel, D. Wilt, M. Dashiell, R. Siergiej, in *AIP Conference Proceedings*, **2004**, *738*, 445.
[13] M. Wanlass, J. Ward, K. Emery, M. Aljassim, K. Jones, T. Coutts, *Sol. Energy Mater. Sol. Cells* **1996**, *41*, 405.
[14] S. Wojtczuk, E. Gagnon, L. Geoffroy, T. Parodos, presented at *AIP Conference Proceedings*, **1995**.
[15] D. M. Wilt, N. S. Fatemi, P. P. Jenkins, V. G. Weizer, R. W. Hoffman Jr., R. K. Jain, C. S. Murray, D. R. Riley, *AIP Conf. Proc.* **1997**, *401*, 237.
[16] Z. Omair, G. Scranton, L. M. Pazos-Outón, T. P. Xiao, M. A. Steiner, V. Ganapati, P. F. Peterson, J. Holzrichter, H. Atwater, E. Yablonovitch, *Proc. Natl. Acad. Sci. U. S. A.* **2019**, *116*, 15356.
[17] K. L. Schulte, R. M. France, D. J. Friedman, A. D. Lapotin, A. Henry, M. A. Steiner, *J. Appl. Phys.* **2020**, *128*, 143103.
[18] D. Fan, T. Burger, S. Mcsherry, B. Lee, A. Lenert, S. R. Forrest, *Nature* **2020**, *586*, 237.
[19] J. G. Cederberg, J. D. Blaich, G. R. Girard, S. R. Lee, D. P. Nelson, C. S. Murray, *J. Crystal Growth* **2008**, *310*, 3453.
[20] J. Schermer, P. Mulder, G. Bauhuis, M. Voncken, J. Van Deelen, E. Haverkamp, P. Larsen, *Phys. Status Solidi* **2005**, *202*, 501.
[21] K. A. Horowitz, T. W. Remo, A. J. Ptak, B. Smith, **2018**, NREL/TP-6A20-72103.
[22] Umicore, https://eom.umicore.com/en/germanium-solutions/products/germanium-substrates/,9/15/23
[23] E. A. Fitzgerald, Y. H. Xie, D. Monroe, P. J. Silverman, J. M. Kuo, A. R. Kortan, F. A. Thiel, B. E. Weir, *J. Vac. Sci. Technol., B* **1992**, *10*, 1807.

© 2024 The Authors. Advanced Energy Materials published by Wiley-VCH GmbH

16146840, 2024, 10, Downloaded from https://onlinelibrary.wiley.com/doi/10.1002/aenm.202303367 by National Renewable Energy Lab Charity Harada, Wiley Online Library on [07/03/2024]. See the Terms and Conditions (https://onlinelibrary.wiley.com/terms-and-conditions) on Wiley Online Library for rules of use; OA articles are governed by the applicable Creative Commons License

[24] K. Mukherjee, D. A. Beaton, A. Mascarenhas, M. T. Bulsara, E. A. Fitzgerald, *J. Crystal Growth* **2014**, *392*, 74.
[25] S. Tomasulo, M. A. Stevens, J. A. Nolde, N. A. Kotulak, M. K. Yakes, *J. Crystal Growth* **2022**, *595*, 126803.
[26] T.-S. Yoon, J. Liu, A. M. Noori, M. S. Goorsky, Y.-H. Xie, *Appl. Phys. Lett.* **2005**, *87*, 012104.
[27] D. Kohen, X. S. Nguyen, R. I. Made, C. Heidelberger, K. H. Lee, K. E. K. Lee, E. A. Fitzgerald, *J. Crystal Growth* **2017**, *478*, 64.
[28] A. Jandl, M. T. Bulsara, E. A. Fitzgerald, *J. Appl. Phys.* **2014**, *115*, 153503.
[29] R. M. France, I. Garcia, W. E. Mcmahon, A. G. Norman, J. Simon, J. F. Geisz, D. J. Friedman, M. J. Romero, *IEEE J. Photovoltaics* **2014**, *4*, 190.
[30] R. M. France, J. F. Geisz, M. A. Steiner, B. To, M. J. Romero, W. J. Olavarria, R. R. King, *J. Appl. Phys.* **2012**, *111*, 103528.
[31] P. M. Mooney, *Mater. Sci. Eng., R* **1996**, *17*, 105.
[32] N. J. Quitoriano, E. A. Fitzgerald, *J. Appl. Phys.* **2007**, *102*, 033511.
[33] K. L. Schulte, H. L. Guthrey, R. M. France, J. F. Geisz, *IEEE J. Photovoltaics* **2019**, *10*, 109.
[34] J. F. Geisz, M. A. Steiner, I. Garcia, R. M. France, W. E. Mcmahon, C. R. Osterwald, D. J. Friedman, *IEEE J. Photovoltaics* **2015**, *5*, 1827.
[35] C.-T. Sah, R. Noyce, W. Shockley, *Proc. IRE* **1957**, *45*, 1228.
[36] J. F. Geisz, R. M. France, K. L. Schulte, M. A. Steiner, A. G. Norman, H. L. Guthrey, M. R. Young, T. Song, T. Moriarty, *Nat. Energy* **2020**, *5*, 326.
[37] W. K. Metzger, M. W. Wanlass, R. J. Ellingson, R. K. Ahrenkiel, J. J. Carapella, *Appl. Phys. Lett.* **2001**, *79*, 3272.
[38] N. Su, P. Fay, S. Sinharoy, D. Forbes, D. Scheiman, *J. Appl. Phys.* **2007**, *101*, 064511.
[39] M. M. A. Gamel, H. J. Lee, W. E. S. W. A. Rashid, P. J. Ker, L. K. Yau, M. A. Hannan, M. Z. Jamaludin, *Materials* **2021**, *14*, 4944.
[40] E. J. Tervo, M. A. Steiner, *Sol. Energy Mater. Sol. Cells* **2022**, *240*, 111735.
[41] H. Iber, E. Peiner, A. Schlachetzki, *J. Appl. Phys.* **1996**, *79*, 9273.
[42] D. Vignaud, J. L. Farvacque, *J. Appl. Phys.* **1989**, *65*, 1261.
[43] J. F. Geisz, D. J. Friedman, M. A. Steiner, R. M. France, T. Song, *IEEE J. Photovoltaics* **2023**, *13*, 808.
[44] H. Helmers, E. Lopez, O. Höhn, D. Lackner, J. Schön, M. Schauerte, M. Schachtner, F. Dimroth, A. W. Bett, *Physica Status Solidi (RRL)–Rapid Research Letters* **2021**, *15*, 2100113.
[45] M. A. Steiner, J. F. Geisz, R. C. Reedy, S. Kurtz, *presented at Photovoltaic Specialists Conference, PVSC'08. 33rd IEEE* **2008**.
[46] K. L. Schulte, R. M. France, H. L. Guthrey, J. F. Geisz, *IEEE J. Photovoltaics* **2018**, *8*, 1349.
[47] N. S. Fatemi, D. M. Wilt, P. P. Jenkins, R. W. Hoffman Jr., V. G. Weizer, C. S. Murray, D. Riley, *AIP Conf. Proc.* **1997**, *401*, 249.

© 2024 The Authors. Advanced Energy Materials published by Wiley-VCH GmbH

16146840, 2024, 10, Downloaded from https://onlinelibrary.wiley.com/doi/10.1002/aenm.202303367 by National Renewable Energy Lab Charity Harada, Wiley Online Library on [07/03/2024]. See the Terms and Conditions (https://onlinelibrary.wiley.com/terms-and-conditions) on Wiley Online Library for rules of use; OA articles are governed by the applicable Creative Commons License